Johann Radon Institute for
Computational and Applied Mathematics
Austrian Academy of Sciences (ÖAW)

Point spread function reconstruction for Single-conjugate Adaptive Optics

R. Wagner, C. Hofer, R. Ramlau

RICAM-Report 2017-46

Point spread function reconstruction for Single-conjugate Adaptive Optics

Roland Wagner[*], Christoph Hofer[†], Ronny Ramlau[‡]

December 21, 2017

Abstract

Modern ground based telescopes like the planned Extremely Large Telescope (ELT) depend heavily on Adaptive Optics (AO) systems to correct for atmospheric turbulence. Even though AO correction is used, the quality of astronomical images still is degraded due to the time delay stemming from the wavefront sensor (WFS) integration time and adjustment of the deformable mirror(s) (DM). This results in a blur which can be mathematically described by a convolution of the original image with the point spread function (PSF).

In this paper, we present an algorithm for SCAO PSF reconstruction adapted to the needs of ELTs in a storage efficient way. In particular, the classical PSF reconstruction algorithm from [21] is changed in several points to give a more accurate estimate for the post-AO PSF. Bilinear splines are used as basis functions in order to minimize the computational effort.

Results obtained in an end-to-end simulation tool show qualitatively good reconstruction of the PSF compared to the PSF calculated directly from the simulated incoming wavefront. Furthermore, the used algorithm has a reasonable run time and memory consumption.

1 Introduction

In ground-based astronomy, the observed image I_o can be described as a convolution of the true image I and the so called point spread function (PSF), i.e.,

$$I_o = I(x) * \mathcal{PSF}(x - y).$$

[*]Johann Radon Institute for Computational and Applied Mathematics, Linz, Austria. roland.wagner@ricam.oeaw.ac.at

[†]Doctoral Program Computational Mathematics, JKU Linz, Austria

[‡]Industrial Mathematics Institute, JKU Linz, Austria, and Johann Radon Institute for Computational and Applied Mathematics, Linz, Austria

The PSF of an astronomical observation through a ground-based telescope depends on the geometry of the telescope and the atmospheric turbulence above the telescope. Modern ground-based telescopes reduce the effect of the turbulent atmosphere by Adaptive Optics (AO) systems. However, still residual turbulences remain uncorrected. The goal is to reconstruct the PSF from data acquired by the wavefront sensors (WFS) and the commands applied to the deformable mirror(s) (DM) after the image has been obtained.

The purpose of this paper is to describe an algorithm for PSF reconstruction in Single-Conjugate Adaptive Optics (SCAO). The PSF of an astronomical image varies with the position in the observed field. As AO corrected images still suffer from the time delay due to the wavefront sensor integration time and adjustment of the deformable mirror(s), the aim is to improve the image quality with deconvolution algorithms where the knowledge of the PSF is required. Furthermore, the PSF can be used to extract estimates for parameters which determine the quality of an astronomical image, e.g., Strehl ratio or Encircled Energy.

PSF reconstruction is based on the WFS data, which is acquired at a frequency of 500 to 3000 Hz. Saving the measured data and performing calculations in a post-processing step will result in an enormous amount of data as the image exposure time ranges from one second to several minutes. In addition, a reconstructed PSF can be used a measure for quality evaluation of the observed image. If the field of view is larger than around 10", knowledge of the PSF in different directions is required, as then the PSF is spatially varying within the field of view.

One major drawback of the upcoming extremely large telescopes (ELT), such as the European ELT, is the relatively coarse resolution of the WFS. This results in a large part of unknown higher order terms of the wavefront. However, the coarse resolution of the WFS becomes necessary due to the faint stars serving as guide stars (GS). Choosing a higher resolution of the WFS would result in having a too low singal to noise ratio in the WFS measurements.

We propose an algorithm for SCAO PSF reconstruction adapted to the needs of ELTs in a storage efficient way. In particular, we adopt the classical PSF reconstruction algorithm from [21], by using a 4D structure function instead of a 2D structure function as well as bilinear basis functions [13, 22]. For bilinear basis functions the higher order aberrations of the atmosphere, i.e., the parts that are not sensed by the WFS, cannot be represented on the same grid as the DM shape. Thus, the higher order terms are simulated and the respective structure functions calculated on a finer grid. Please not that higher order aberrations can only be estimated from simulations as they are not

available even for real telescope data. Furthermore, a model of the noise influencing the measurements has to be available. All proposed steps are done for closed loop AO systems.

Our approach is in contrast to other proposed methods such as [9], which takes a maximum likelihood approach for the used covariance matrices, or [17], where only open loop data is taken into account and a fine resolution WF is created by combining measurements from different timesteps. Some of the algorithms were already successfully tested on sky on various telescopes [15, 14, 10, 6, 16]. Algorithms for PSF reconstruction in SCAO suffer from anisoplanatism. An approach to overcome these difficulties has been presented in [4, 1]. It can be combined with our algorithm in order to obtain PSFs for each point in the field of view. In [5] an $\ell^1 - \ell^2$ model for PSF reconstruction is proposed to create high resolution phase gradients from subsequent WFS frames and obtain an estimate of the instantaneous PSF when no AO correction is used. As pointed out in [7], prior to the reconstruction algorithms the PSF of a reference star was measured from a separate observation directly before or after the science observation and then used for deconvolution algorithms. However, this approach implicitly uses the strong assumptions that the atmospheric conditions are sufficiently stable and that the flux and intensity on the WFS is the same for the PSF reference star and the target's guide star.

In the following Section, we recall the original algorithm from [21] and highlight some of its limits for reconstructing the PSF from WFS data. We present our new approach in Section 3. Section 4 shows results obtained with ESO's end-to-end simulation tool Octopus.

2 PSF reconstruction for SCAO

In order to have a good understanding of existing algorithms, we review Véran's algorithm, first presented in [21].

2.1 Reconstructing the PSF from WFS data: Véran's algorithm

The instantaneous optical transfer function (OTF), denoted by B, in the near field approximation for a monochromatic image at wavelength λ is given in [21] as

$$B(\boldsymbol{\rho}/\lambda, t) = \frac{1}{S} \int_{\mathcal{P}} P(\mathbf{x}) P(\mathbf{x} + \boldsymbol{\rho}) \exp\left(i\phi(\mathbf{x}, t)\right) \exp\left(-i\phi(\mathbf{x} + \boldsymbol{\rho}, t)\right) d\mathbf{x}, \tag{1}$$

where S is the area of the telescope aperture and ϕ is the residual phase after the AO correction. The normalization ensures that the PSF has unit energy. Note that the dependence on the wavelength λ is implicit through the relation between phase ϕ and wavefront

φ as $\phi(x,t) = \frac{2\pi}{\lambda}\varphi(x,t)$. Averaging the instantaneous OTF over the integration time interval gives the long exposure OTF.

Furthermore, assuming that the corrected phase at any position on the pupil has a Gaussian statistics and the integration time is long enough, so that the statistical average can be substituted by the temporal average, leads to the following expression of the long exposure OTF:

$$B(\boldsymbol{\rho}/\lambda) = \langle B(\boldsymbol{\rho}/\lambda, t)\rangle_t = \frac{1}{S}\int_{\mathcal{P}} P(\mathbf{x})P(\mathbf{x}+\boldsymbol{\rho})\exp\left(-\frac{1}{2}D_\phi(\mathbf{x},\boldsymbol{\rho})\right)d\mathbf{x}, \tag{2}$$

where the structure function of the residual incoming phase is

$$D_\phi(\mathbf{x},\boldsymbol{\rho}) = \langle|\phi(\mathbf{x},t) - \phi(\mathbf{x}+\boldsymbol{\rho},t)|^2\rangle_t,$$

with $\langle\cdot\rangle_t$ the temporal average of a function. Then, one can obtain the long exposure PSF by applying the Fourier transform to the long exposure OTF, keeping the wavelength λ fixed, i.e.,

$$\mathcal{PSF}(\mathbf{u}) = \mathcal{F}(B(\boldsymbol{\rho}/\lambda)). \tag{3}$$

It is suggested in [21] to replace $D_\phi(\mathbf{x},\boldsymbol{\rho})$ by its mean over $\mathbf{x}$, i.e.,

$$\bar{D}_\phi(\boldsymbol{\rho}) = \frac{\int_{\mathcal{P}} P(\mathbf{x})P(\mathbf{x}+\boldsymbol{\rho})D_\phi(\mathbf{x},\boldsymbol{\rho})d\mathbf{x}}{\int_{\mathcal{P}} P(\mathbf{x})P(\mathbf{x}+\boldsymbol{\rho})d\mathbf{x}}, \tag{4}$$

which is equivalent to assuming that the disperion in $\mathbf{x}$ is small enough that the exponential of the mean can be approximated by the mean of the exponential and leads to an under-estimation of the OTF since the exponential is a convex function. This simplifies the calculations now as only averaging over two-dimensional functions is required. Furthermore, with the orthogonal splitting of the residual incoming phase into a component in the space spanned by the mirror modes $\phi_\parallel$ and into a higher order component $\phi_\perp$, i.e., $\phi = \phi_\parallel + \phi_\perp$,

$$\begin{aligned}\bar{D}_\phi(\boldsymbol{\rho}) &= \bar{D}_{\phi_\parallel}(\boldsymbol{\rho}) + \bar{D}_{\phi_\perp}(\boldsymbol{\rho}) \\ &\quad + 2\frac{\int_{\mathcal{P}} P(\mathbf{x})P(\mathbf{x}+\boldsymbol{\rho})\langle[\phi_\parallel(\mathbf{x},t) - \phi_\parallel(\mathbf{x}+\boldsymbol{\rho},t)][\phi_\perp(\mathbf{x},t) - \phi_\perp(\mathbf{x}+\boldsymbol{\rho},t)]\rangle_t d\mathbf{x}}{\int_{\mathcal{P}} P(\mathbf{x})P(\mathbf{x}+\boldsymbol{\rho})d\mathbf{x}},\end{aligned} \tag{5}$$

where the last (cross) term is neglected although it is not rigorously zero due to potential correlation through the remaining error. With these simplifications we get

$$B(\boldsymbol{\rho}/\lambda) = \underbrace{\exp\left(-\frac{1}{2}\bar{D}_{\phi_\parallel}(\boldsymbol{\rho})\right)}_{B_\parallel(\boldsymbol{\rho}/\lambda)}\underbrace{\exp\left(-\frac{1}{2}\bar{D}_{\phi_\perp}(\boldsymbol{\rho})\right)}_{B_\perp(\boldsymbol{\rho}/\lambda)}\underbrace{\int_{\mathcal{P}} P(\mathbf{x})P(\mathbf{x}+\boldsymbol{\rho})d\mathbf{x}}_{B_{tel}(\boldsymbol{\rho}/\lambda)}, \tag{6}$$

where $\bar{D}_{\phi_\parallel}$ and $\bar{D}_{\phi_\perp}$ are defined as in (4).

Now these three parts can be reconstructed separately: $B_\parallel$ can be estimated from control loop AO data, $B_\perp$ can be estimated from simulated data only and B_{tel} is given analytically. The first two terms clearly depend on the seeing conditions of the current observation. Therefore an algorithm to estimate the seeing from AO loop data was developed. The quantity $B_\perp$ has to be simulated only once and can then be scaled to the current observing conditions.

To be able to compute $\bar{D}_{\phi_\parallel}(\boldsymbol{\rho})$ fast, Véran introduced functions $U_{ij}(\boldsymbol{\rho})$ that depend on the possible mirror modes and can be precomputed numerically. For the remaining calculation only the time averaged covariances of the WFS data are needed. As the original algorithm was proposed for Zernike polynomials, this method turned out to give good results, but still was time and memory consuming. Therefore, [11] diagonalized Véran's approach using so called V_{ii}-functions, where an eigenvalue decomposition of the computed covariance matrix is needed, which gives a speed up for certain basis functions.

For the computation of $\bar{D}_{\phi_\perp}(\boldsymbol{\rho})$, a Monte Carlo method is proposed, where the high order components of randomly generated phase screens with Kolmogorov or Van Karman statistics are extracted and then using a temporal and spatial average for the structure function.

2.2 Limits of PSF reconstruction from WFS data

Clearly the accuracy of PSF reconstruction from WFS data is limited by the hardware of the telescope. Due to the coarse resolution of the WFS, the part of $\phi_\parallel$ has its limit at the WFS cut off frequency and thus gives only a rather coarse estimate for the structure function.

As the WFS are not perfect devices, it holds that $\Gamma\phi_\perp \neq 0$, where Γ is the Shack-Hartmann WFS operator, that maps incoming wavefronts to measurements. This influences the reconstructed wavefronts and/or atmospheric layers and as a result changes $D_{\phi_\parallel}$ slightly. In addition to that there is some measurement noise in $\Gamma\phi$, leading to further changes in the structure function. The latter one can be modeled and thus corrected if one has a good knowledge on the WFS.

For good estimates of $D_{\phi_\perp}$, the seeing parameter r_0 (or D/r_0) is needed for the calculation of $\phi_\perp$ and for estimating the influence of $\Gamma\phi_\perp$ on the PSF. A good estimate can be obtained by using, e.g., the iterative procedure from [21, Section 3.2.3].

When going on sky with a PSF reconstruction algorithm, one has to adjust for non-common path aberrations, as the optical path to the WFS and the science camera are not the same. In the algorithm above this means that B_{tel} is not only calculated from the pupil function, but can be calibrated in form of a static PSF as the non-common path aberrations are static. Note that the adjustments necessary to compensate for this effect can be obtained via calibration as the non-common path aberrations are static at much longer time scales than atmospheric aberrations.

3 Novel approach to PSF reconstruction for SCAO

Since the proposal of Véran's algorithm in [21], computational power and available memory increased, therefore some adjustments of the algorithm to improve the quality are possible in feasible computational time. In particular it was never demonstrated that Zernike polynomials as basis functions are an appropriate choice for modern deformable mirrors with completely different influence functions. Furthermore, the required computational power for Zernike polynomials is rather high due to their global support, which results in full and dense matrices. We want to use basis functions with local support in order to reduce the computational complexity and to be able to account for the four dimensionality of the structure function.

3.1 Updating PSF reconstruction for SCAO

We start from (2), i.e.,

$$B(\boldsymbol{\rho}/\lambda) = \frac{1}{S}\int_{\mathbb{R}^2} P(\mathbf{x})P(\mathbf{x}+\boldsymbol{\rho})e^{-\frac{1}{2}D_\phi(\mathbf{x},\boldsymbol{\rho})}\,d\mathbf{x},$$

where $D_\phi(\mathbf{x},\boldsymbol{\rho}) = \langle|\phi(\mathbf{x},t)-\phi(\mathbf{x}+\boldsymbol{\rho},t)|^2\rangle$, and make some adjustments. The exact calculation of $B(\boldsymbol{\rho}/\lambda)$ requires averaging four dimensional functions, which seemed computationally too demanding when Véran developed his algorithm and thus proposed to interchange spatial average and the exponential function to overcome this problem. Nowadays this simplification can be partly dropped, as these computations are possible in reasonable time even on a laptop as shown, e.g., in [12].

As a starting point of our approach, we split ϕ into a part seen by the WFS (and thus corrected by the DM in the following time step), called $\phi_\parallel$, and a part orthogonal to the DM modes, called $\phi_\perp$. Clearly, $\phi = \phi_\parallel + \phi_\perp$ and thus

$$D_\phi(\mathbf{x},\boldsymbol{\rho}) = D_{\phi_\parallel}(\mathbf{x},\boldsymbol{\rho})+D_{\phi_\perp}(\mathbf{x},\boldsymbol{\rho})+2\langle[\phi_\parallel(\mathbf{x},t)-\phi_\parallel(\mathbf{x}+\boldsymbol{\rho},t)][\phi_\perp(\mathbf{x},t)-\phi_\perp(\mathbf{x}+\boldsymbol{\rho},t)]\rangle_t. \quad (7)$$

Note that in [21] this splitting was made after interchanging spatial average and the exponential.

The last term is a cross term between differences of two orthogonal terms and is not rigorously zero because $\phi_{\parallel}$ and $\phi_{\perp}$ may be correlated through the remaining error. However, according to [21] it can be assumed that it is negligible. Thus, the OTF can be rewritten as

$$B(\boldsymbol{\rho}/\lambda) = \frac{1}{S}\int_{\mathcal{P}} P(\mathbf{x})P(\mathbf{x}+\boldsymbol{\rho})\exp\left(-\frac{1}{2}D_{\phi_{\parallel}}(\mathbf{x},\boldsymbol{\rho})\right)\exp\left(-\frac{1}{2}D_{\phi_{\perp}}(\mathbf{x},\boldsymbol{\rho})\right)d\mathbf{x}. \tag{8}$$

The orthogonal part of the residual phase cannot be measured from the actual on sky data, but only simulated offline by using sophisticated atmospheric models. Therefore, using one realization of $\phi_{\perp}$ for the calculation of $D_{\phi_{\perp}}(\mathbf{x},\boldsymbol{\rho})$ gives no meaningful contribution and we follow partly the suggestion of [21] to replace it by $\bar{D}_{\phi_{\perp}}(\boldsymbol{\rho})$, its mean over the variable $\mathbf{x}$ given by

$$\bar{D}_{\phi_{\perp}}(\boldsymbol{\rho}) = \frac{\int_{\mathcal{P}} P(\mathbf{x})P(\mathbf{x}+\boldsymbol{\rho})\exp\left(-\frac{1}{2}D_{\phi_{\perp}}(\mathbf{x},\boldsymbol{\rho})\right)d\mathbf{x}}{\int_{\mathcal{P}} P(\mathbf{x})P(\mathbf{x}+\boldsymbol{\rho})d\mathbf{x}},$$

so that (2) simplifies to

$$B(\boldsymbol{\rho}/\lambda) = \frac{1}{S}\exp\left(-\frac{1}{2}\bar{D}_{\phi_{\perp}}(\boldsymbol{\rho})\right)\int_{\mathcal{P}} P(\mathbf{x})P(\mathbf{x}+\boldsymbol{\rho})\exp\left(-\frac{1}{2}D_{\phi_{\parallel}}(\mathbf{x},\boldsymbol{\rho})\right)d\mathbf{x}, \tag{9}$$

which is a product of two independent terms. The first term can be estimated only from simulation, as $\phi_{\perp}$ is not available on sky and the second term has to be calculated on the fly from closed loop AO measurements. Note that, when using the original method from [21], also the structure function of $\phi_{\parallel}$ is averaged over $\mathbf{x}$, which results in three independent components: the OTF of the telescope in absence of turbulence, the contribution of the mirror component and the contribution of the higher order phase. In our approach however, the first two components are combined into one.

3.2 Changing the basis functions

As Zernike polynomials have global support, the calculations in the U_{ij}-algorithm requires the assembling of full matrices, which leads to increased memory consumption and computational power. Due to the high degrees of freedom for the future ELTs this is not feasible. In particular, if one considers the use of linear influence functions for future DMs, one could think of using, e.g., bilinear splines as basis functions for the U_{ij}-algorithm as proposed in [13]. This change leads to a sparse representation of the needed matrices for the mirror part, but the higher order terms cannot be represented well as the coefficients correspond to the evaluation of the wavefront in the actuator positions, which should not

contain a higher order part, when correcting the atmosphere perfectly.

To overcome this problem, we use a finer resolution of the wavefronts for the estimation of the higher order parts. As a drawback this results in higher memory consumption and slower computations. Since the higher order components $\phi_\perp$ are precomputed and appropriately scaled to current observation conditions, this is not a crucial issue with modern computers.

3.3 Using wavefronts instead of WFS measurements

In the original algorithm from [21], the WFS measurements were used as a starting point and all calculations were based directly on the WFS measurements. However, the structure function of an AO run, D_ϕ, is directly related to the incoming wavefronts. As the incoming wavefronts are reconstructed to obtain the shape of the DM, we propose to use these reconstructions directly for the estimation of D_ϕ.

For an SCAO system, commonly matrix-vector-multiplication (MVM) is used for the reconstruction process. Recently, matrix free algorithms, such as CuReD [24, 19, 20], HWR [2], both tested on sky [3], and FinECuReD [18, 23], were introduced. Thus, starting from reconstructed wavefronts instead of WFS measurements does not increase the computational complexity. Certain effects such as sensor noise still have to be modeled on measurement level and then transferred onto the wavefront level, but these are computations which can be done prior to the AO and PSF reconstruction run and therefore have no effect on the run time.

4 Numerical results

In this section we present some further details on the estimation of the structure function of the higher order components of the incoming phase $\bar{D}_{\phi_\perp}$ as well as symmetry considerations which are used reduce memory consumption during run time. Furthermore, results for PSF reconstruction in an SCAO system are shown for different guide star flux and the influence of reduced input data is investigated.

4.1 High order components of the incoming phase

In order to reconstruct the PSF properly we need to have an estimate for $\bar{D}_{\phi_\perp}$. This estimate can only be obtained by simulation, in our case using OCTOPUS. As a feature, OCTOPUS provides the possibility to save incoming phase screens and the residual screens after AO correction. The same procedure is possible for computed DM updates

and also for the actual DM shapes.

In a naive approach, one would use the residual phase screens ϕ_n^{res} after AO correction, which already gives reasonable results. However, due to the time lag of the AO system ϕ_n^{res}, where n indicates the time step in simulation, still contains the information used for ϕ_{n+1}^{DM}, the DM update at time step $n+1$, which is clearly a part of $\phi_\parallel$ and not of $\phi_\perp$. To eliminate this influence, we use for the calculation of $\bar{D}_{\phi_\perp}$ the following formula

$$\phi_{\perp,n} = \phi_n^{res} + \phi_{n+1}^{DM},$$

using the fact that the DM update has the opposite sign of the incoming phase as it corrects for these distortions. Note that this means that $\phi_{\perp,n}$ is not only the projection on the perpendicular space of the DM influence functions, but also contains the reconstruction error in the space of DM influence functions. This leads to a dependence of $\phi_{\perp,n}$ on the reconstruction quality and thus on the photon flux from the guide star.

In order to avoid temporal correlation in $\bar{D}_{\phi_\perp}$, we perform the temporal average not over every $\phi_{\perp,n}$, but take only every 5th of these residual phases. Additionally, we downsample the residual phase to bigger pixel size as otherwise calculating the structure function would be computationally too heavy. In this downsampling procedure, the choice of the basis functions for numerical implementation plays a crucial role. If one wants to choose a basis built up by bilinear splines, calculating $\bar{D}_{\phi_\perp}$ on the same grid as the DM updates (and WFS measurements) will not be successful. The main reason for this is that a DM with linear influence functions is able to perfectly correct for bilinear splines. Thus a finer grid for the calculation of $\phi_{\perp,n}$, and therefore $\bar{D}_{\phi_\perp}$ is needed. Results are provided for pixel sizes $\delta x = \frac{1}{k} d_{DM}$, with $k = 2, 4, 8$, where d_{DM} is the spacing of the DM actuators, and in our simulations also the size of one WFS subaperture.

Note, that the c_n^2-profile used for the simulation is not changing and will in reality not perfectly match with the one during observation.

The orthogonal part of the phase $\phi_\perp$ is simulated with a photon flux of 1000 photons/subaperture/frame. We use two seconds of real time for estimating the structure function of the orthogonal part $\bar{D}_{\phi_\perp}$, but take only every 10th time frame to reduce temporal correlation. OCTOPUS has a parameter called *turbulent_seed*, defining the starting point for the generation of atmospheric layers in a pseudo-random way. In order to avoid an unrealistic setting, we take different values of *turbulent_seed* for estimating $\bar{D}_{\phi_\perp}$ and the on-the-fly computation for estimating $D_{\phi_\parallel}$. In particular, this prevents that $\bar{D}_{\phi_\perp}$ and $D_{\phi_\parallel}$ match perfectly for the used atmosphere. However, using the same atmospheric profile still is a very optimistic approach.

4.2 Setting for numerical simulations

To verify that the proposed algorithm works well, we tested it in ESO's end-to-end simulation tool OCTOPUS for a planned ELT SCAO setting using WFS data from one NGS observed with a 74×74 SH-WFS running at wavelength $\lambda = 0.7\ \mu m$ and a science wavelength $\lambda = 2.2\ \mu m$. The decision for using OCTOPUS is based on the quest for a simulation tool where one can extract the generated incoming wavefront to get a reference PSF calculated directly from the wavefront residual after the DM correction. Such a reference PSF is needed in order to compare the reconstructed PSF to the true solution of the reconstruction problem. OCTOPUS can directly provide such PSFs for specified directions.

The atmosphere used for the tests is the proprietary ELT ESO atmosphere with 10 layers and a seeing $r_0 = 12.1$ cm at 500 nm. To get a better view on the effects of guide stars with different brightness on the PSF, the tests are performed for different photon flux from the NGS, but during one test run the flux is fixed. The photon flux varies for all tests between 100 and 1000 photons/subaperture/time frame. We do not consider noise coming from the detector read out and the incoming photons. Each simulation represents two seconds of real time, i.e., 1000 time steps of the simulation are performed with an WFS integration time of 2 ms. An overview of the simulated system is presented in Table 1. Note that the WFS setting stems from a preliminary design for the METIS instrument at the ELT, but a similar setting is also planned for the MICADO instrument. For reconstructing the incoming wavefront, and thus controlling the DM, CuReD (cf, [24, 19]) is used.

Telescope diameter	37 m
central obstruction	10.36 m
1 NGS Shack-Hartmann WFS	74×74 subapertures
WFS wavelength λ	$0.7\ \mu m$
WFS integration time	2 ms
1 DM at height 0 m	closed loop
DM actuator spacing	0.5 m
science wavelength λ	$2.2\ \mu m$
Simulation time	2 s real time (1000 time steps)

Table 1: Description of the simulated SCAO system

4.3 Numerical results for high photon flux

We investigate the high flux case with $n_{ph} = 1000$, i.e., 1000 photons reach each subaperture in every time step in the setting of Table 1. In Figure 1, we compare cuts through

the x-axis of the PSF reconstructed by our algorithm and the PSF calculated by ESO's OCTOPUS simulation tool. The latter one is a reference as it is calculated directly from the simulated atmosphere and averaged over time. However, both PSFs are in the plane of the WFS and not in the plane of the science image, but still at the science wavelength of 2.2 μm. This means that the simulation does not account for non common path errors of the system. Furthermore, also effects of the telescope, such as jitter, are not simulated. A good agreement between the reconstructed and the true PSF can be seen in the core, whereas the wings are overestimated in the reconstructed version and show a different structure. These differences are not crucial as most energy is in the core and the values decay fast with increasing distance to the center. The overestimation of the wings is a drawback of the coarse spatial resolution of the reconstructed phase $\phi_{\parallel}$ and also of the orthogonal part $\phi_{\perp}$.

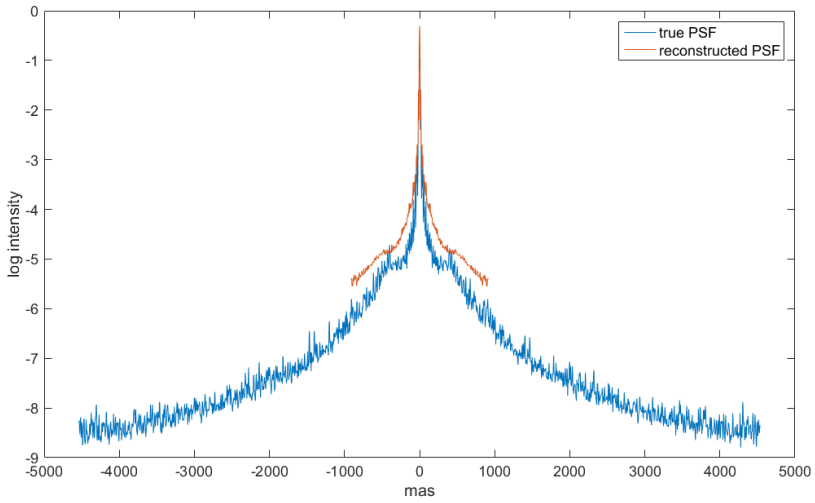

Figure 1: Comparison of the true PSF (blue) and the reconstructed PSF (red) for $n_{ph} = 1000$, cut through the main diagonal.

For many scientists the center of the PSF is of most interest, therefore we show a zoom in Figure 2 to highlight the differences between the reconstructed and the true PSF. From the PSF several parameters can be deduced, for example the Strehl ratio. As the Strehl ratio relates the peaks of the seeing limited PSF and the diffraction limited PSF, dividing the peak of the reconstructed PSF by the peak of the true PSF gives the accuracy of the Strehl ratio, i.e.,

$$\frac{|SR_{true} - SR_{rec}|}{SR_{true}},$$

where SR_{true} and SR_{rec} are the Strehl ratios calculated from the true and the reconstructed PSF, respectively. Note, that without particular tuning of the loop gain, the

used AO control algorithm, CuReD [24, 19], reaches a Strehl ratio of 77.9%. In our computations, we find that the peak (and thus the Strehl ratio) is underestimated by 3.2%, i.e., our reconstructed PSF suggests a Strehl ratio of only 75.4%.

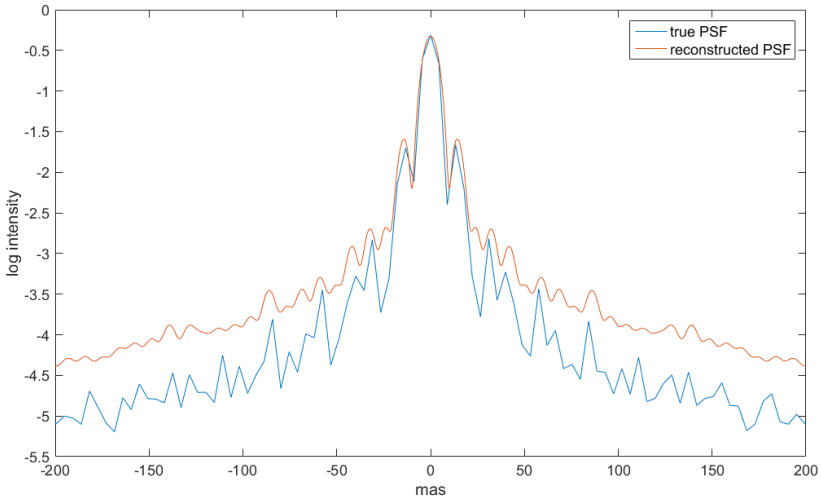

Figure 2: Zoom to the center of the true PSF (blue) and the reconstructed PSF (red) for $n_{ph} = 1000$, cut through the main diagonal.

4.3.1 Influence of the resolution of $\phi_\perp$

As described in Section 4.1, $\phi_\perp$ and the corresponding structure function can only be obtained from simulations. Therefore the quest for a suitable spatial resolution of $\phi_\perp$ arises. This resolution should not be too coarse on the one hand, meaning that this would not give more details than the WFS data themselves. On the other hand, a too fine resolution leads to enormous consumption of memory and computational power. From the fact that a phase ϕ and its $\mathcal{PSF}$ are related through the Fourier transform, one can deduce a relation between the spatial resolution of ϕ, δx, given in m/pixel, and the resolution of $\mathcal{PSF}$, $\delta\omega$, in radians, as

$$N_{pix} \cdot \delta x \cdot \delta\omega = 2\pi,$$

where N_{pix} is the number of pixels in $\mathcal{OTF}$, or similarly $\mathcal{PSF}$, along one axis. This is an elementary consideration of the fact that quantities appearing in the exponential have to be dimensionless. Translating δx from units m/pixel to 1/pixel, introduces a factor $2\pi/\lambda$, being then wavelength dependent. For obtaining a resolution in *mas* one has to divide by $4.85 \cdot 10^{-9}$, which is the conversion factor between radians and mas.

Using the above formula, one can see that refining δx does not lead to a finer resolution $\delta\omega$, as with such a refinement also N_{pix} increases by the same factor. Thus a finer δx corresponds to adding parts in the wings of the $\mathcal{PSF}$. We demonstrate this fact in Figure 3, comparing the resolution PSFs for $(\delta x)_1 = 0.25\ m$, $(\delta x)_2 = 0.125\ m$ and $(\delta x)_3 = 0.0625\ m$. It is clearly visible, that the wings of the PSF are resolved further outside. Also in the part already resolved with $(\delta x)_1$ an improvement is visible as for $(\delta x)_2$ and $(\delta_x)_3$ the reconstructed PSF shows less overestimation (see Figure 4). This is a result of the fact, that the PSFs are normalized in L^2 in order to be energy preserving in image (de-)convolution.

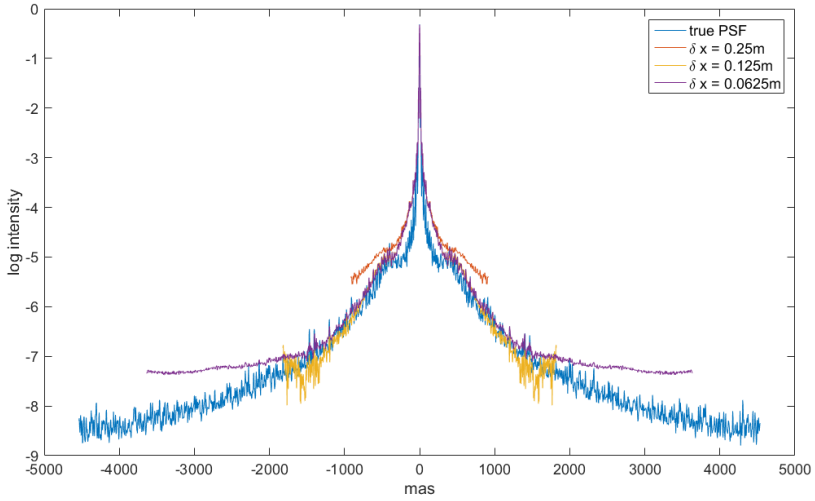

Figure 3: Comparison of the true PSF (blue), the reconstructed PSF with $\delta x = 0.25\ m$ (red), $\delta x = 0.125\ m$ (yellow) and $\delta x = 0.0625\ m$ (purple) for $n_{ph} = 1000$, cut through the main diagonal.

Again, we compare the peaks of the true and the reconstructed PSFs. For $(\delta x)_1$, the peak is underestimated by 3.3% and, for $(\delta x)_2$, the underestimation reduces to 3%. For $(\delta x)_3$, we get another gain to 2.7%.

Note that the resolution of $\phi_{\|}$ is always limited by the size of the WFS subapertures. Therefore, the corresponding $\mathcal{OTF}_{\|}$ has to be interpolated onto the finer grid used in the simulations for $\phi_{\perp}$ in order to obtain the correct dimensions. This interpolation is done linearly with the in-built `MATLAB`-function *interp2*.

4.3.2 Influence of 2D and 4D structure function

In Section 3.1, we modified the PSF reconstruction for SCAO by using a 4D structure function $D_{\phi_{\|}}(x, \rho)$ instead of the 2D version used in Véran's algorithm. We now want to

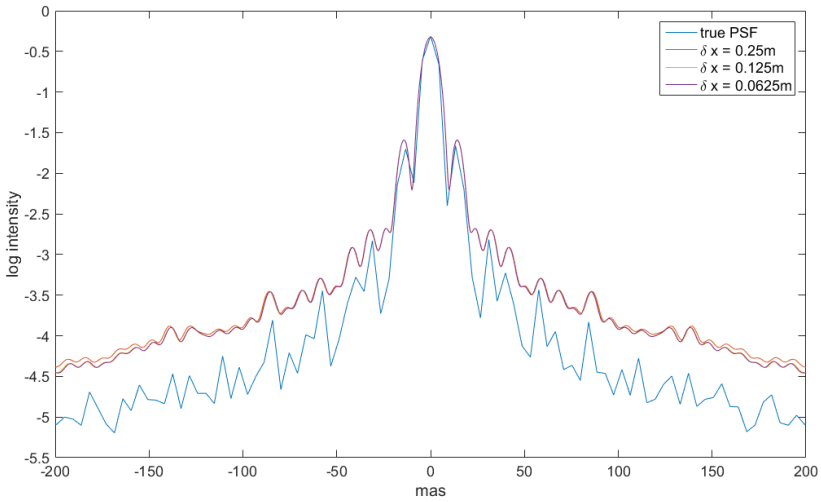

Figure 4: Zoom to the center of the comparison of the true PSF (blue), the reconstructed PSF with $\delta x = 0.25\ m$ (red), $\delta x = 0.125\ m$ (yellow) and $\delta x = 0.0625\ m$ (purple) for $n_{ph} = 1000$, cut through the main diagonal.

compare the effect of using these two different versions of the structure function. Clearly, the 4D version is computationally more demanding, but still can be computed in reasonable time on a modern computer.

The result when using the above high flux setting, with a spatial resolution of $\delta x = 0.25\ m$, is shown in Figure 5. We found that the reconstruction of the PSF core is slightly improved when using the 4D structure function instead of the 2D, but the decay in the wings shows some rapid drops from 10^{-6} to 10^{-10} before rising again. The decay in the wings is not as expected and the reason are computational instabilities as the values in the structure function are close to machine precision. However, comparing the Strehl ratios leads to an improvement from an error of 3.3% with the 2D structure function to an error of 2% error with the 4D structure function. Zooming into the center (see Figure 6) highlights another improvement in the first PSF ring, which is less overestimated using a 4D structure function.

We also investigated the impact of using the two different versions of the structure function for $\delta x = 0.125\ m$. The results are similar, therefore we omit additional figures. The error in the Strehl ratio is 3% for the 2D structure function and only 1.7% for the 4D structure function. Using $\delta x = 0.0625\ m$, there is little improvement in the error for the 2D version to 2.7%, and the error in the Strehl ratio reduces to 1.5% for the 4D structure function. In Figure 7 we display a comparison of the 4D structure function calculated with different resolutions δx.

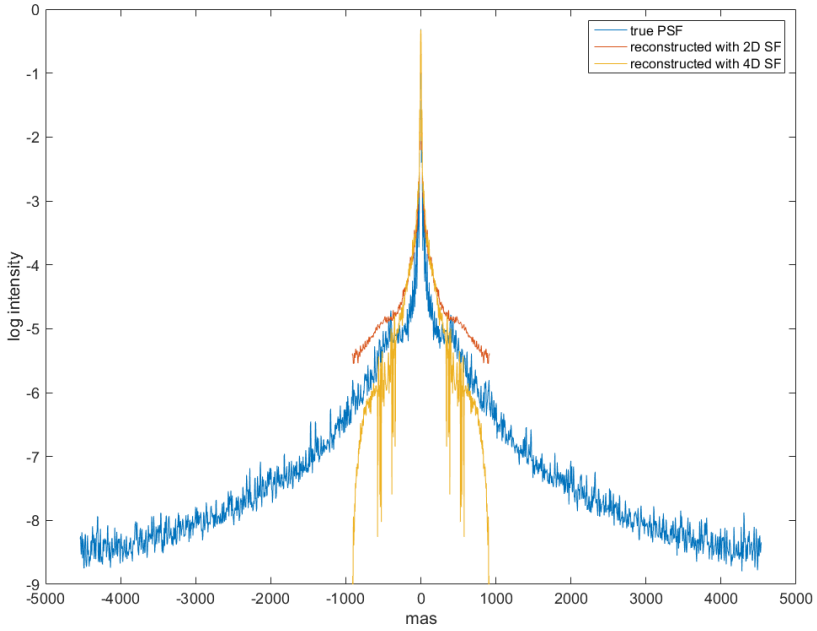

Figure 5: Comparison of the true PSF (blue), the reconstructed PSF with a 2D structure function (red) and 4D structure function (yellow) for $n_{ph} = 1000$, cut through the main diagonal.

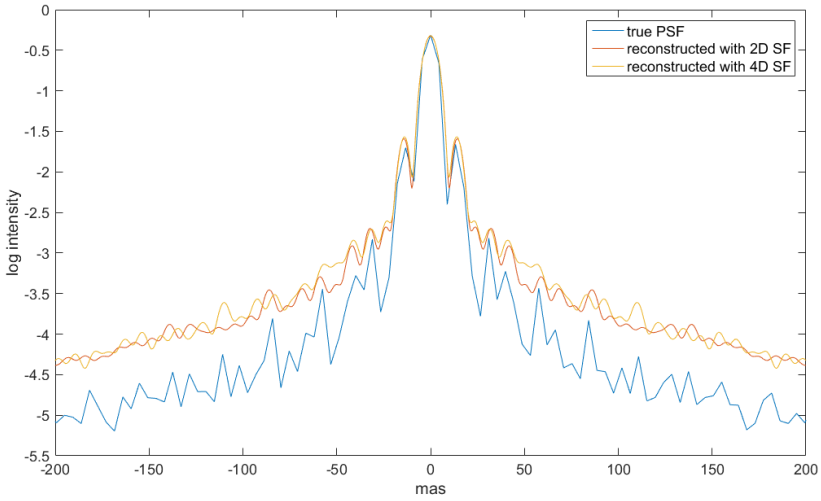

Figure 6: Zoom to the center of the comparison of the true PSF (blue), the reconstructed PSF with $\delta x = 0.25\ m$ using a 2D structure function (red) and a 4D structure function (yellow) for $n_{ph} = 1000$, cut through the main diagonal.

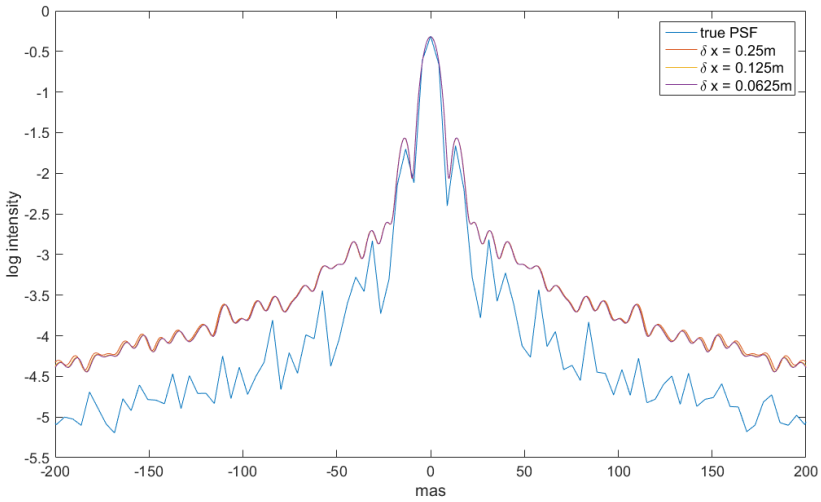

Figure 7: Zoom to the center of the comparison of the true PSF (blue), the reconstructed PSF using the 4D structure function with $\delta x = 0.25\ m$ (red), $\delta x = 0.125\ m$ (yellow) and $\delta x = 0.0625\ m$ (purple) for $n_{ph} = 1000$, cut through the main diagonal.

4.4 Numerical results for low photon flux

In the previous subsections we considered a fixed physical setup and varied some computational parameters. In real observations also the physical setup, mainly the photon flux coming from the guide star, will vary from one observation to another. In particular, certain observations will require the use of faint guide stars. Therefore, the proposed algorithm should give reliable results also for lower photon flux.

The telescope and simulation setup remains as in Table 1. For this section we also fix the photon flux to 1000 photons/subaperture/frame in the simulation of $\bar{D}_{\phi_\perp}$ and test both versions, the 2D and the 4D structure function, for $\phi_\parallel$. Furthermore, the c_n^2-profile remains constant. Note that using a higher photon flux in the simulation part will result in higher errors as this neglects that with decreasing photon flux also the quality of the AO control decreases. However, performing simulations for all levels of photon flux at different resolutions will result in extensive computations.

Figure 8 shows the reconstructed PSF and the true PSF for $n_{ph} = 500$. The Strehl ratio calculated from OCTOPUS is 77.4%. As in the high flux case, the difference between the true and the reconstructed PSF is small and the Strehl ratio is estimated very well. Using a 4D structure function the error in the Strehl ratio decreases from 3.6% for $\delta x = 0.25\ m$ to 3% for $\delta x = 0.0625\ m$, in the 4D version, and is thus in the same regime as for the high flux case. Using the 2D structure function gives a quality loss compared to the high

flux case and results in errors for the Strehl ratio ranging from 4% for $\delta x = 0.25\ m$ to 3.5% for $\delta x = 0.0625\ m$.

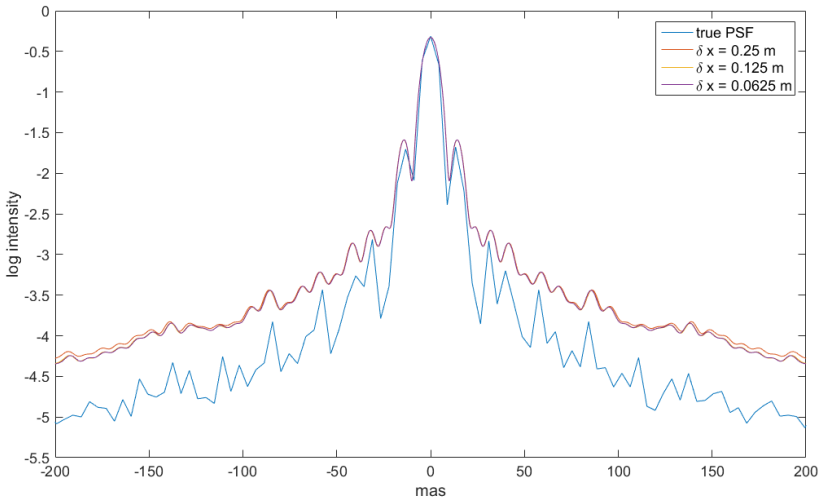

Figure 8: Zoom to the center of the comparison of the true PSF (blue) and the reconstructed PSF with $\delta x = 0.25\ m$ (red), $\delta x = 0.125\ m$ (yellow) and $\delta x = 0.0625\ m$ (purple) for $n_{ph} = 500$, cut through the main diagonal.

Reducing the flux further to $n_{ph} = 100$ gives the results displayed in Figure 9 and a drop of the Strehl ratio to 73%. For our simulation setting, we obtain an error in Strehl ratio of 8.7% for $\delta x = 0.25\ m$ and 8.2% for $\delta x = 0.0625\ m$. When using the 2D structure function, the increase of the error compared to higher flux is smaller as the error in the Strehl ratio lies between 4.1% and 4.6% for the different discretizations. This might be an effect from using a simulation with high flux for the calculation of $\bar{D}_{\phi_\perp}$, as this structure function depends also on the reconstruction quality of $\phi_\parallel$ (see Section 4.1).

5 Conclusion and outlook

In this work we presented an algorithm for PSF reconstruction in an SCAO system for the upcoming generation of ELTs. In contrast to Véran's algorithm, our approach is based on wavefronts rather than on measurements and uses the 4D structure function. First simulations show qualitatively good reconstruction of the PSF compared to the PSF calculated directly from the simulated incoming wavefront. Furthermore, the used algorithm has a reasonable run time and memory consumption.

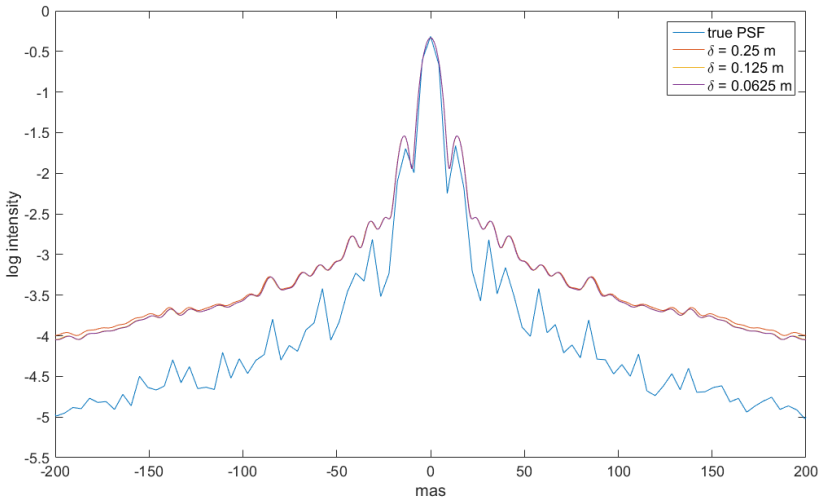

Figure 9: Zoom to the center of the comparison of the true PSF (blue) and the reconstructed PSF with a 2D structure function for $\delta x = 0.25\ m$ (red), $\delta x = 0.125\ m$ (yellow) and $\delta x = 0.0625\ m$ (purple) for $n_{ph} = 100$, cut through the main diagonal.

The algorithm can be further improved by a more accurate model for the noise covariance used in $D_{\phi_\parallel}$.

Future goals, are to develop a version of the proposed algorithm which can be used for PSF reconstruction in a multi-conjugate adaptive optics (MCAO) system, where PSF knowledge across the whole field of view is required an can be obtained using measurements from all GS.

Additionally, we want to use the reconstructed PSFs as input in a blind deconvolution algorithm for image improvement, which can be done after the observation on the telescope. Such an approach leads to a further improvement of the quality of the reconstructed PSF and simultaneously improves the quality of the observed image. First results for a simplified setting can be found, e.g., in [8].

Acknowledgments

The work of RW and RR was funded by the Hochschulraumstrukturfonds of the Austrian Ministry of research (bmwfw) in the project “Beobachtungsorientierte Astrophysik in der E-ELT Ära”. The work of CH was funded by the Austrians Science Fund (FWF) in the grant W1214, project DK 4. This support is gratefully acknowledged.

References

[1] M. Aubailly, M. Roggemann, and T. Schulz. "Approach for reconstructing anisoplanatic adaptive optics images". In: *Applied Optics* 46.24 (2007), pp. 6055–6063. DOI: 0003-6935/07/246055-09$15.00/0.

[2] N. Bharmal, U. Bitenc, A. Basden, R. Myers, and N. Dipper. "A hierarchical wavefront reconstruction algorithm for gradient sensors". In: *Third AO4ELT Conference – Adaptive Optics for Extremely Large Telescopes*. 2013. DOI: 10.12839/AO4ELT3.13280.

[3] U. Bitenc, A. Basden, N. Ali Bharmal, T. Morris, N. Dipper, E. Gendron, F. Vidal, D. Gratadour, G. Rousset, and R. Myers. "On-sky tests of the CuReD and HWR fast wavefront reconstruction algorithms with CANARY". In: *Monthly Notices of the Royal Astronomical Society* 448.2 (2015), pp. 1199–1205.

[4] M.C. Britton. "The Anisoplanatic Point Spread Function in Adaptive Optics". In: *Publications of the Astronomical Society of the Pacific* 118.844 (2006), pp. 885–900. DOI: 10.1086/505547.

[5] R. Chan, X. Yuan, and W. Zhang. "Point spread function reconstruction in ground-based astronomy by l1-lp model". In: *JOSA A* 29 (2012), pp. 2263–2271.

[6] Y. Clénet, C. Lidman, E. Gendron, G. Rousset, T. Fusco, N. Kornweibel, M. Kasper, and N. Ageorges. "Tests of the PSF reconstruction algorithm for NACO/VLT". In: *Proc. SPIE 7015, Adaptive Optics Systems, 701529*. 2008. DOI: 10.1117/12.789395.

[7] R. Davies and M. Kasper. "Adaptive Optics for Astronomy". In: *Annual Review of Astronomy and Astrophysics* 50 (2012), pp. 305–351. DOI: 10.1146/annurev-astro-081811-125447.

[8] L. Dykes, R. Ramlau, L. Reichel, K.M. Soodhalter, and R. Wagner. "Lanczos-based fast blind deconvolution methods". In: *RICAM Report* 2017-27 (2017).

[9] J. Exposito, D. Gratadour, G. Rousset, Y. Clénet, E. Gendron, and L. Mugnier. "A new method for adaptive optics point spread function reconstruction". In: *Third AO4ELT Conference – Adaptive Optics for Extremely Large Telescopes*. 2013. DOI: 10.12839/AO4ELT3.13328.

[10] R.C. Flicker. "PSF reconstruction for Keck AO: Phase 1 Final Report". In: *W.M. Keck Observatory, 65-1120 Mamalahoa Hwy., Kamuela, HI 96743, USA* (2008).

[11] E. Gendron, Y.Clénet, T.Fusco, and G. Rousset. "New algorithms for adaptive optics point-spread function reconstruction". In: *Astronomy & Astrophysics* 457.1 (2006), pp. 359–463. DOI: 10.1051/0004-6361:20065135.

[12] L. Gilles, C. Correia, J.-P. Véran, L. Wang, and B. Ellerbroek. "Simulation model based approach for long exposure atmospheric point spread function reconstruction for laser guide star multiconjugate adaptive optics". In: *Applied Optics* 51.31 (2012), pp. 7443–7458.

[13] C. Hofer. "Point spread function reconstruction for singleconjugated adaptive optics systems". MA thesis. Johannes Kepler University Linz, 2014.

[14] L. Jolissaint, J. Christou, P. Wizinowich, and E. Tolstoy. "Adaptive optics point spread function reconstruction: lessons learned from on-sky experiment on Altair/Gemini and pathway for future systems". In: *Proc. SPIE 7736, Adaptive Optics Systems II, 77361F*. 2010. DOI: 10.1117/12.857670.

[15] L. Jolissaint, C. Neyman, J. Christou, P. Wizinowich, and L. Mugnier. "First Successful Adaptive Optics PSF Reconstruction at W. M. Keck Observatory". In: *Proc. SPIE 8447, Adaptive Optics Systems III, 844728*. 2012. DOI: 10.1117/12.926607.

[16] O. A. Martin, C. M. Correia, E. Gendron, G. Rousset, D. Gratadour, F. Vidal, T. J. Morris, A. G. Basden, R. M. Myers, B. Neichel, and T. Fusco. "PSF reconstruction validated using on-sky CANARY data in MOAO mode". In: *Proc. SPIE 9909, Adaptive Optics Systems V*. 2016.

[17] J. Nagy, S. Jefferies, and Q.Chu. "Fast PSF reconstruction using the frozen flow hypothesis". In: *Proceedings of the Advanced Maui Optical and Space Surveillance Technologies Conference*. 2010.

[18] A. Neubauer. "A new cumulative wavefront reconstructor for the Shack-Hartmann sensor". In: *J. Inv. Ill-Posed Problems* 21 (2013), pp. 451–476.

[19] M. Rosensteiner. "Cumulative Reconstructor: fast wavefront reconstruction algorithm for Extremely Large Telescopes". In: *J. Opt. Soc. Am. A* 28.10 (2011), pp. 2132–2138.

[20] M. Rosensteiner. "Wavefront reconstruction for extremely large telescopes via CuRe with domain decomposition". In: *J. Opt. Soc. Am. A* 29.11 (2012), pp. 2328–2336.

[21] J.-P. Véran, F. Rigaut, H. Maître, and D. Rouan. "Estimation of the adaptive optics long exposure point spread function using control loop data". In: *J. Opt. Soc. Am. A* 14.11 (1997), pp. 3057–3069. DOI: 10.1364/JOSAA.14.003057.

[22] R. Wagner. "From Adaptive Optics systems to Point Spread Function Reconstruction and Blind Deconvolution for Extremely Large Telescopes". PhD thesis. Johannes Kepler University Linz, 2017.

[23] R. Wagner, A. Neubauer, and R. Ramlau. "Simulation results for a finite element-based cumulative reconstructor". In: *Journal of Astronomical Telescopes, Instruments, and Systems* 3.4 (2017), p. 049001. DOI: 10.1117/1.JATIS.3.4.049001.

[24] M. Zhariy, A. Neubauer, M. Rosensteiner, and R. Ramlau. “Cumulative Wavefront Reconstructor for the Shack-Hartman Sensor”. In: *Inverse Problems and Imaging* 5.4 (2011), pp. 893–913.